AIAA JOURNAL
Vol. 33, No. 5, May 1995

Numerical Behavior of Unsteady Waves

S. Aubert,* L. Hallo,† P. Ferrand,‡ and M. Buffat§
Ecole Centrale de Lyon, Ecully 69131, France

Two unsteady Euler solvers using high-order upwind finite volume methods are presented and compared. The first uses the Van Leer flux vector splitting on structured moving grids and includes compatibility relations to treat boundary conditions. The second is based on Roe's approximate Riemann solver on fixed unstructured, finite element type meshes and uses a standard explicit boundary treatment. Results for one- and two-dimensional strong wave propagation and interaction show very good agreement between the two approaches and reference solutions, despite the use of different flux evaluations and integration cells. The two schemes even exhibit the same numerical sensitivity of wave propagation to mesh orientation. However, the simulation of the shock wave reflection from a wall reveals some flaws in the second solver's slip wall treatment which are avoided by the compatibility relations used in the first method.

Nomenclature

A	= Jacobian matrix of F
$\boldsymbol{F}$	= inviscid flux vector
F	= numerical flux, $\boldsymbol{F} \cdot \boldsymbol{n}\, dS$
J	= Jacobian of coordinate transformation matrix
$k(j)$	= list of neighboring nodes of node j
L	= left eigenvectors of A written as line
$\boldsymbol{n}$	= unit normal vector
q	= column vector of conservative variables
Q	= interpolation of q along S
S	= boundary surrounding Ω
t	= time
V	= modulus of velocity
Δt	= time step
ξ^1, ξ^2, ξ^3	= curvilinear coordinates
Ω	= volume of integration

Subscripts

j	= nodal point index
jk	= pertaining to the edge connecting node j to node k

Superscripts

j	= pertaining to ξ^j direction
(n)	= time level
$+/-$	= forward/backward extrapolation or splitting

I. Introduction

MANY practical external or internal transonic flow problems involve complex patterns of waves. These can result from wakes or shocks interacting with each other or from the reflection of waves from a solid boundary. The flow can be either steady or unsteady, with stationary or traveling waves. Such situations appear, for example, with helicopter rotors where waves generated by a blade interact with the following blade, or in turbomachinery where rotor/stator interactions occur. A further example is where flutter, the coupling between wave motion and structure deformation, can lead to the destruction of the structure. Along with the problems related to measurement in high-speed flows, this last example reveals why it is easier and safer to study such phenomena numerically instead of using experimental investigations.

Since the early days of computational fluid dynamics (CFD), numerous approaches were developed to handle discontinuities arising in unsteady transonic flows. In the last decade, great improvements have been made. An extensive survey of the state-of-the-art high-resolution schemes has been made by Yee,[1] and an excellent review on upwind conservative shock-capturing methods is given by Roe.[2] From these two pieces of literature it is apparent that a finite volume formulation is one of the best available solutions.

According to these considerations, we have developed two methods, which differ in the long term aim, but which seem well suited to simulate transient waves in a perfect gas. The first approach is designed to compute three-dimensional unsteady flows in turbomachinary where interactions of waves and aeroelastic coupling between flow and blades occurs. It is based on a monotonic upwind-centered scheme for conservation laws (MUSCL) finite volume formulation[3] on moving structured meshes. It uses the Van Leer flux vector splitting technique with the Mulder limiter.[4] Boundary conditions are implemented by means of compatibility relations, using the interior time scheme.[5] The time discretization involves the explicit forward Euler formula. The whole scheme is built to ensure coherence in time with particular attention being paid to avoiding numerical phase differences for the transient solution. It is subsequently referenced as PROUST. The aim of the second method is to provide a means of predicting steady two-dimensional internal transonic flows in combustion chambers. To take into account complex geometries and to allow local grid refinement, unstructured finite element meshes are used. The finite volume integration cells are built around each node by means of the medians.[6] The approximate Riemann solver of Roe with the Van Albada limiter is employed.[7] Since this scheme is designed for steady-state solutions, quite simple explicit boundary conditions are implemented, which tend to introduce phase differences. For moderate time steps, however, this method should be able to treat unsteady discontinuities. It is subsequently referenced as NATURng.

The approaches share the same philosophy. However, spatial discretizations, flux evaluations, and boundary treatments differ. This study explains briefly how each scheme is implemented and presents a comparison of results for one- and two-dimensional wave interactions. The aim is to judge if one scheme is consistently better than the other.

II. Numerical Discretization

In their integral form, the governing equations for a perfect gas are

$$\int_{\Omega(t)} \frac{\partial q}{\partial t}\, d\Omega + \oint_{S(t)} \boldsymbol{F}(q) \cdot \boldsymbol{n}\, dS = 0 \qquad (1)$$

Received Nov. 3, 1992; revision received Aug. 25, 1994; accepted for publication Sept. 14, 1994.

*Lecturer, Université Claude Bernard-Lyon 1, Laboratoire de Mécanique des Fluides et d'Acoustique, URA CNRS 263, ECL-BP 163.

†Ph.D. Student, Université Claude Bernard-Lyon 1, Laboratoire de Mécanique des Fluides et d'Acoustique, URA CNRS 263, ECL-BP 163.

‡Research Associate, Université Claude Bernard-Lyon 1, Laboratoire de Mécanique des Fluides et d'Acoustique, URA CNRS 263, ECL-BP 163.

§Professor, Université Claude Bernard-Lyon 1, Laboratoire de Mécanique des Fluides et d'Acoustique, URA CNRS 263, ECL-BP 163.

These state that the rate of change of the conservative variables in a finite volume is balanced by the flux crossing its bounding surface. The expressions of q and $\boldsymbol{F}$ can be found in many references and will not be repeated here.

From this point, the two numerical procedures presented follow a standard finite volume formulation. First, the flowfield is discretized using cells at the center of which the spatial average of conservative variables is stored. Then the flux is evaluated using a reconstruction of the variable field along $S(t)$ from the cell-average values, using upwind schemes. A time stepping procedure finally produces the time evolution of q. Details are given next.

PROUST: a Van Leer Scheme on Structured Meshes

In this approach, the three-dimensional computational domain is divided into a structured mesh comprised of hexahedra, moving in Cartesian space, but steady and cubic in the curvilinear frame. Integration cells are thus cubes of unit edge centered on nodes. The cell faces are located at $\xi^j \pm \frac{1}{2}$ (Fig. 1). The discretized expression relating to Eq. (1) is

$$\frac{\partial}{\partial t}(Jq)\bigg|_{\xi^1,\xi^2,\xi^3} + \sum_{j=1}^{3}\left[F^j\left(\xi^j + \tfrac{1}{2}\right) - F^j\left(\xi^j - \tfrac{1}{2}\right)\right] = 0 \qquad (2)$$

where F^j includes a contribution due to the movement of the cell interface.[8]

To evaluate F^j, Van Leer's flux vector splitting is applied.[4] Using a MUSCL approach,[3] two states separated by the cell interface, Q^{j-} and Q^{j+}, are interpolated from the cell-center values. The numerical flux is written as

$$F^j = F^{j+}(Q^{j-}) + F^{j-}(Q^{j+}) \qquad (3)$$

where, for example, the forward flux F^{j+} is expressed as a function of the backward interpolated variable Q^{j-}.

To construct high-order schemes, a piecewise linear distribution of conservative flow variables over each cell is assumed to reconstruct the $Q^{j\pm}$ states at each cell face. However, to avoid oscillations at discontinuities such as shocks, and to ensure monotonicity, the amplitude of the local gradients is constrained within some bounds. The Mulder limiter[9] was chosen to adjust locally the interpolation order of each $Q^{j\pm}$ component. Thus,

$$\begin{aligned} Q^{j-}\left(\xi^j - \tfrac{1}{2}\right) &= Q(q_{\xi^j}, q_{\xi^j-1}, q_{\xi^j-2}) \\ Q^{j+}\left(\xi^j - \tfrac{1}{2}\right) &= Q(q_{\xi^j-1}, q_{\xi^j}, q_{\xi^j+1}) \end{aligned} \qquad (4)$$

where $Q(q_a, q_b, q_c)$ represents the extrapolation in ξ^j direction of the cell-center value q_b, along the slope $(q_b - q_c)$, limited by the relative steepness of the $(q_a - q_b)$ and $(q_b - q_c)$ gradients. A tuning of q_a, q_b, and q_c weighting coefficients in the expression for Q controls the interpolation accuracy.

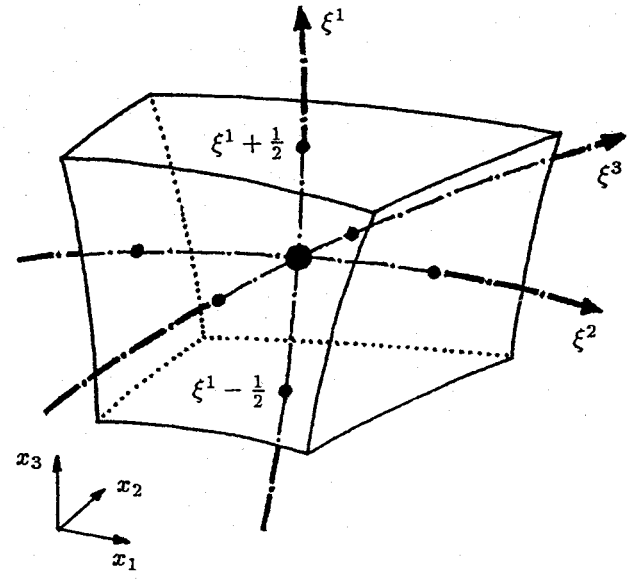

Fig. 1 PROUST structured integration cell.

NATURng: a Roe Scheme on Unstructured Meshes

To deal with complex geometries and to allow local grid refinement, the two-dimensional flowfield for this method is discretized using triangles to form a steady unstructured mesh. For each node j, the integration cell is defined as the union of the quadrangles including j, built from the subdivision of a triangle by means of its medians[10] (Fig. 2). The face combining the two segments connected to an edge jk defines the contribution in $\boldsymbol{n}_{jk}$ direction to the bounding surface. Equation (1) is thus rewritten as

$$\Omega_j \cdot \frac{\partial q_j}{\partial t} + \sum_{k=k(j)} F_{jk} = 0 \qquad (5)$$

To evaluate F_{jk}, Roe's approximate Riemann solver is applied locally at each cell face.[7] As previously, two discrete states separated by the cell interface, Q_{jk} and Q_{kj}, are first interpolated using the nodal values. The numerical flux is obtained as

$$F_{jk} = \tfrac{1}{2}[F(Q_{jk}) + F(Q_{kj})] - \tfrac{1}{2}|A_{jk}|(Q_{jk} - Q_{kj}) \qquad (6)$$

where A_{jk} is evaluated using Roe's average fluid state from Q_{jk} and Q_{kj}.

A piecewise linear distribution of primitive variables over each cell is assumed to reconstruct the Q_{jk} states, except in the vicinity of flow discontinuities where a constant value per cell is assumed. The Van Albada limiter[11] provides a sensor for such features, giving a smooth transition between the different order of interpolation regions. Q_{jk} is evaluated as

$$Q_{jk} = Q(q_j, q_k, \nabla q_j \cdot \boldsymbol{n}_{jk}) \qquad (7)$$

where ∇q_j is computed using a standard finite element approximation over linear triangles. Equation (7) represents the extrapolation in the $\boldsymbol{n}_{jk}$ direction of the cell-center value q_j, along the slope $\nabla q_j \cdot \boldsymbol{n}_{jk}$, limited by the relative steepness of the $(q_k - q_j)$ and $2\nabla q_j \cdot \boldsymbol{n}_{jk} - (q_k - q_j)$ gradients.

Time Integration

The two semidiscrete forms Eqs. (2) and (5) can be summarized as

$$\frac{\partial Q}{\partial t} = -R(Q) \qquad (8)$$

where R includes the space terms previously described by Eqs. (3) and (6).

The time scale of the physical phenomena encompassed by this paper (e.g., the free propagation of a shock wave) is often comparable with the time step determined by numerical stability

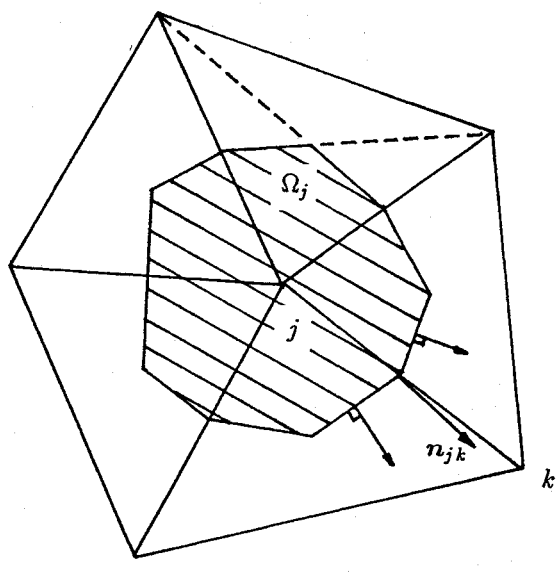

Fig. 2 NATURng unstructured integration cell.

constraints.[12] An explicit time discretization is, therefore, suitable. The simplest of these is doubtless the Euler scheme, which is a first-order accurate forward integration obtained as

$$Q^{(n+1)} - Q^{(n)} = -\Delta t R(Q^{(n)}) \tag{9}$$

Under the classical Courant–Friedrichs–Lewy (CFL) condition, such a method is stable, because of the total variation diminishing properties of the schemes used to compute the space terms.[13]

III. Boundary Treatment

The unsteady flowfields presented in this paper are bounded either by slip walls or by symmetry planes. Simulations are stopped before the waves reach either inflow or outflow boundaries, or at least, before reflected information corrupts the region of interest. Special inlet and outlet treatments are therefore not required.

PROUST Boundary Treatment

In the structured approach, distinction is made between geometrical conditions, such as symmetry, and physical conditions, such as slip walls. For symmetry planes, two extra layers of nodes for which the Euler equations are not solved are built around the computational domain. Coordinates and flow variables at these new vertices are obtained from geometrical relations. In this way, the points on a symmetry plane are treated as interior points. Consistency in time is thus achieved.

At slip boundaries, compatibility relations are used to take into account physical boundary conditions. The technique used has been detailed by Hirsch.[5] Waves crossing a constant ξ^i border are described by premultiplying the Euler equations by the left eigenvectors of the Jacobian matrix of F^i. In this new set of equations, the outgoing characteristics are retained, since these provide information from inside the domain. The incoming characteristics, on the other hand, are replaced by physical boundary conditions. To do so, the slip condition $V^i = 0$ is recast as a first-order partial differential equation in time using a Taylor expansion

$$\left[\frac{\partial V^i}{\partial (Jq)}\right]^{(n)} \frac{\partial}{\partial t}(Jq) = -\frac{1}{\Delta t} V^{i(n)} \tag{10}$$

Thus Eq. (2), projected onto the characteristic surface, is combined with Eq. (10) to give

$$[P^1]\frac{\partial}{\partial t}(Jq) + [P^2]\sum_{j=1}^{3}\left[F^j\left(\xi^j + \tfrac{1}{2}\right) - F^j\left(\xi^j - \tfrac{1}{2}\right)\right] = [P^3] \tag{11}$$

where

$$P^1 = \begin{bmatrix} \cdots L^{i,1} \cdots \\ \cdots L^{i,2} \cdots \\ \cdots L^{i,3} \cdots \\ \cdots L^{i,4} \cdots \\ \cdots \dfrac{\partial V^i}{\partial (Jq)} \cdots \end{bmatrix} \tag{12}$$

$$P^2 = \begin{bmatrix} \cdots L^{i,1} \cdots \\ \cdots L^{i,2} \cdots \\ \cdots L^{i,3} \cdots \\ \cdots L^{i,4} \cdots \\ \cdots 0 \cdots \end{bmatrix} \tag{13}$$

$$P^3 = \begin{bmatrix} 0 \\ 0 \\ 0 \\ 0 \\ -\dfrac{V^i}{\Delta t} \end{bmatrix} \tag{14}$$

with, for example, $L^{i,1}$ being the left eigenvector relating to the first outgoing characteristic.

Finally, Eq. (11), premultiplied by $[P^1]^{-1}$, is solved at a boundary node and is integrated in time in the same way as Eq. (2) for an interior point. Fluxes parallel to the boundary surface are calculated in the same way as inside the domain. The F^i flux, normal to the wall, is evaluated using a complete flux expression, without splitting, with flow variables on one side extrapolated from the interior of the domain.

NATURng Boundary Treatment

On unstructured meshes, only the slip condition has been implemented to compute the results presented. Symmetry planes were thus modeled as flat slip walls. Zero mass flow is imposed for solid boundaries, which implies that the convective flux in Eq. (5), between a boundary node j and the computational domain outside $F_{j\infty}$, is a function of the static pressure p_j only.[14] The value of p_j corresponds to an equilibrium pressure, which maintains the fluid within the domain. From a numerical point of view, the value at the previous time step is used. This approximation does not affect the steady state but is significant for unsteady flows. The calculated pressure ensures consistency with conservation in the Euler equations but is potentially a crude estimate of the equilibrium pressure, even with small time steps.

Considering Eq. (5) for a boundary node, the F_{jk} fluxes are calculated using Roe's flux expression. The $F_{j\infty}$ flux is evaluated using a complete flux expression.

IV. Numerical Results

One-Dimensional Wave Interactions

The problem computed involves two shock tubes, sharing the same low-pressure chamber (Fig. 3). Initially, pressure and density ratios are the same across the two diaphragms. Temperature is uniform, and the gas is at rest. Just after the two diaphragms have been broken, shock waves and contact discontinuities move toward the center of the tube, whereas expansion waves travel outwards. As a result of the initial conditions, the pattern is symmetric about the center of the tube. Between time 0.20 s and 0.40 s, the interaction of the two pressure waves generates two reflected shocks. Then, at about 0.50 s, the reflected pressure waves encounter the contact discontinuities. Reflected and transmitted shocks are generated, and the contact surface is deflected. The two reflected pressure waves move toward the center of the tube and interact again to give two new reflected shocks. Further interactions obviously take place but are not studied here. With such a flow, we are investigating how numerical methods deal with the interaction of one-dimensional strong waves of various strengths.

The initial conditions chosen are a pressure and a density ratio of 4 between high- and low-pressure chambers. The pressure to density ratio is 1, and the velocity is 0. The tube extends from -1.0 to 1.0, and is divided into 200 equal cells. The initial diaphragm positions are -0.495 and 0.495. The time step is constant and fixed at 1.10^{-3} s. Under such conditions, the initial shock wave, which is the fastest wave, needs six time steps to cross one cell (CFL $\leq \frac{1}{6}$).

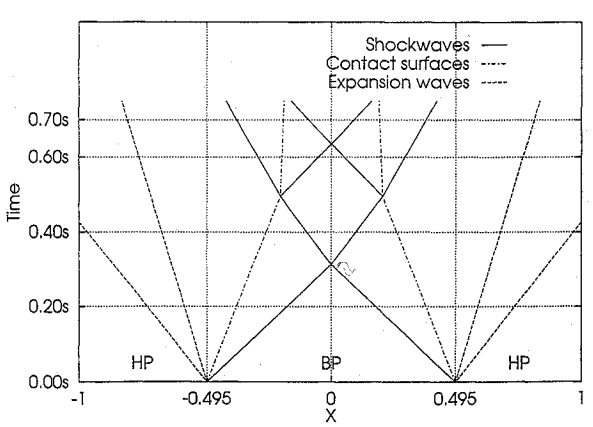

Fig. 3 Theoretical pattern of wave interactions.

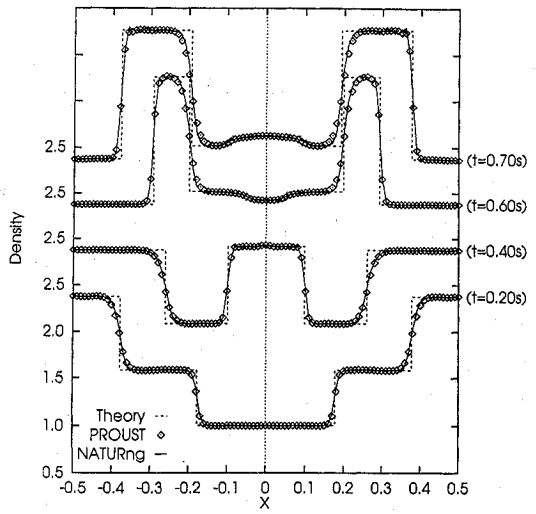

Fig. 4 One-dimensional density profiles.

The exact solution of this gas dynamic flow problem is known, and is used as a reference.[15]

Density profiles are given at time $t = 0.20$ s, 0.40 s, 0.60 s, and 0.70 s, before and after each interaction in Fig. 4. The behavior of rarefaction waves is of no interest, so profiles are restricted to $-0.5 \leq X \leq 0.5$. At $t = 0.20$ s, the results are in close agreement with those expected for a single shock tube problem. Pressure waves moving toward $X = 0.0$ may be identified, followed by the contact discontinuities. At $t = 0.3122$ s, there is an interaction between the shocks, and two reflected pressure waves moving outwards are generated. They are visible at $t = 0.40$ s on each side of $X = 0.0$, whereas contact discontinuities are still moving toward the center of the tube. At $t = 0.4955$ s, interactions take place between the reflected shocks and the contact surfaces. Reflected and transmitted pressure waves appear, and the contact discontinuity is deflected. At $t = 0.60$ s, the reflected shocks are near $X = 0.0$, whereas the contact surfaces are at $X = -0.2$ and 0.2. The transmitted shocks are moving outwards. The last interaction occurs at $t = 0.6357$ s between the two reflected pressure waves. Two small shocks moving outwards are generated. They are visible at $t = 0.70$ s on each side of $X = 0.0$.

We notice that throughout the computation, the two methods give the right position and strength of each wave, even after several interactions. The difference between the two numerical solutions is small. However, the NATURng profiles for contact discontinuities are slightly sharper, but the difference is marginal. All shocks remain smeared over 3–4 cells, whereas contact discontinuities are smeared over 7–8 cells. The smoothing of discontinuities does not increase when interactions occur. Even the last shocks, which are very weak, are captured with the right theoretical level.

The solution is fully symmetric about $X = 0.0$. The interaction of two shocks at the center is thus equivalent to the reflection of one shock from a solid boundary. To simulate this situation, the computation is repeated, keeping the right-hand side and placing a wall at $X = 0.0$.

We deal only with the first shock interaction. Density profiles are presented at $t = 0.40$ s in Fig. 5 near the end wall. Profiles obtained after the interaction of two symmetric shocks are included. The PROUST boundary treatment produces results close to those obtained with two shocks. The density level at the wall is accurately computed, even if the only imposed boundary condition is that the velocity vanishes for $X = 0.0$. On the other hand, the NATURng profile oscillates slightly, with the density overestimated at wall. It was observed that this overshoot decreases with time to reach the theoretical level. This behavior is related to the wall pressure whose previous time step value is used to enforce the slip condition. This phase lag thus affects the shock/wall interaction even with CFL $\leq \frac{1}{6}$. (Another well-known technique to estimate the wall pressure is to extrapolate a value from within the domain. It exascerbates the problem, however, as it results in mingling of information from different time levels). However, the problem is restricted to the vicinity of the boundary nodes, and the numerical solutions remain fairly near one another elsewhere, and close to the exact solution.

Two-Dimensional Wave Interactions

The converging cylindrical shock problem is considered next. In this two-dimensional test case, a cylindrical diaphragm initially separates two perfect gases at rest. The external pressure and density are higher than the internal ones. Along a diameter, initial profiles of density, momentum, and energy are the same as those just described for the one-dimensional case. After the diaphragm is broken, however, the traveling waves are cylindrical and not plane. The sequence of events is the same, but the times and levels differ because of axisymmetric influences. This configuration is used to investigate the motion and interaction of two-dimensional strong waves.

The initial conditions are as in the previous test case. The physical domain is a square of edge 2.0, centered on zero. The diaphragm is situated at $r = 0.495$. The computational mesh covers a quarter of the space, $(X, Y) \in [0.0; 1.0]^2$, with symmetry conditions applied on the axes. There are 101 points with constant spacing in both directions. The time step was again set at 1.10^{-3} s. No exact solution is available, but the idealized physical problem has been treated numerically by a number of researchers.[16–19] The numerical results of Zhang and So[19] which are typical are used as a reference.

The contour plots of density predicted by PROUST are shown in Figs. 6–10. At $t = 0.00$ s, the diaphragm is broken. As time increases, a shock and a contact discontinuity appear, moving toward the center (Fig. 6). At $t \simeq 0.30$ s, the shock reaches the origin and becomes a singular point with high levels of pressure and density (Fig. 7). A reflected shock is then generated moving outwards (Fig. 8). At $t \simeq 0.50$ s, it interacts with the contact discontinuity (Fig. 9). Reflected converging and transmitted diverging pressure waves appear, whereas the contact discontinuity is altered and deflected outwards (Fig. 10).

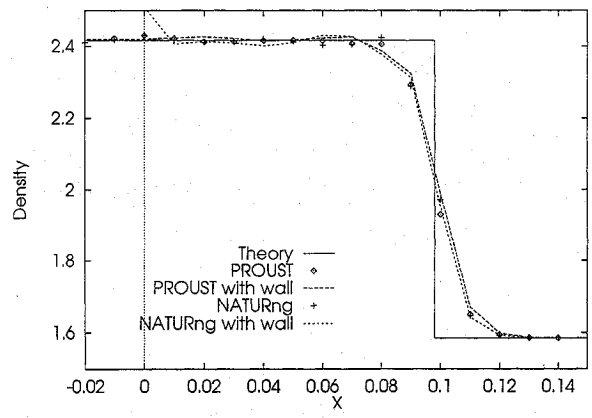

Fig. 5 One-dimensional density profiles near end-wall at $t = 0.40$ s.

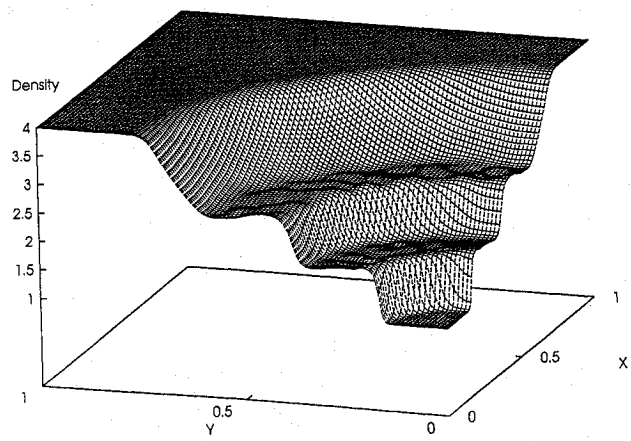

Fig. 6 Density contour in one quadrant at $t = 0.20$ s (PROUST).

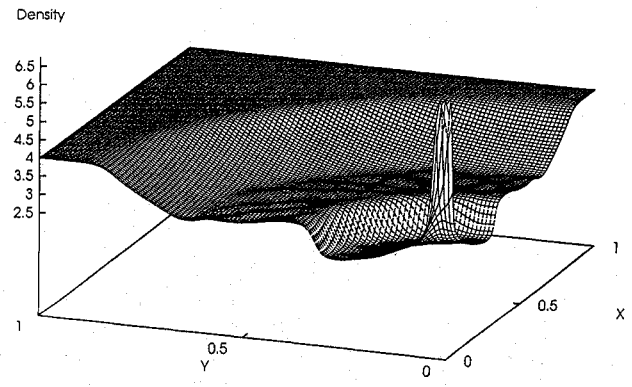

Fig. 7 Density contour in one quadrant at t = 0.30 s.

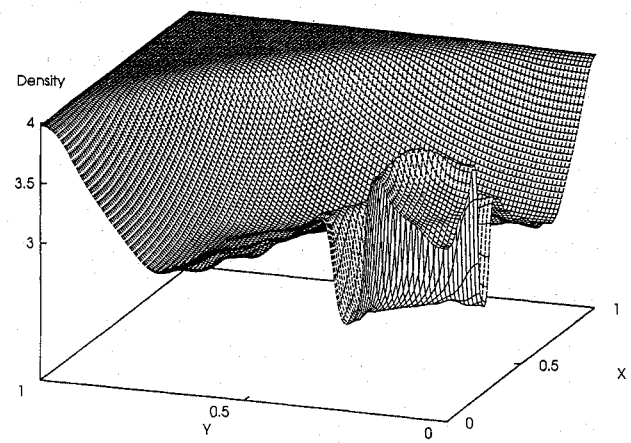

Fig. 8 Density contour in one quadrant at t = 0.40 s.

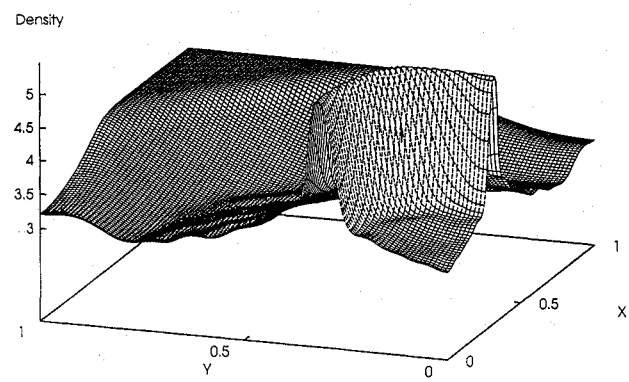

Fig. 9 Density contour in one quadrant at t = 0.50 s.

Density profiles along the diagonal of the square computed with PROUST and NATURng are superimposed in Figs. 11 and 12. The unsteady behavior is qualitatively similar to that depicted for the one-dimensional case (Fig. 4), but the levels between the waves are no longer constant because of angular confining. The two methods lead to similar solutions throughout the computation. Quantitative comparisons with the numerical results of Zhang and So[19] show good agreement, with an improved shock resolution, but a spreading of the contact discontinuity. The overestimation by NATURng of the density level at the center is again related to the slip condition treatment as explained previously for the one-dimensional reflection from a wall. However, this does not disturb the solution generally.

Undesirable ripples following the traveling waves may be noted in Fig. 6, where levels constant in the angular direction are expected. These ripples are also present in the NATURng results (Fig. 13), and in Zhang and So.[19] From our experience, this is due to the relative orientation of a moving discontinuity compared to the borders of an integration cell. As mentioned by Hirsch,[20] the one-dimensional

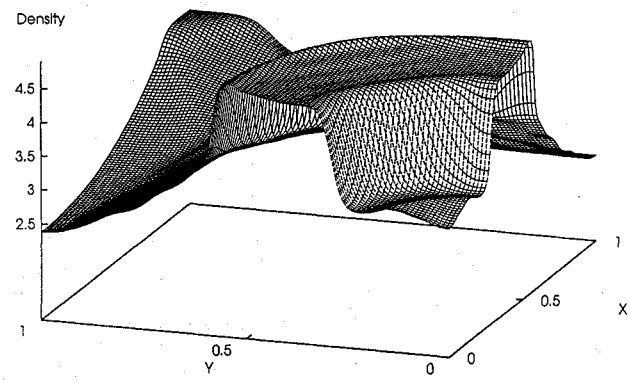

Fig. 10 Density contour in one quadrant at t = 0.70 s (PROUST).

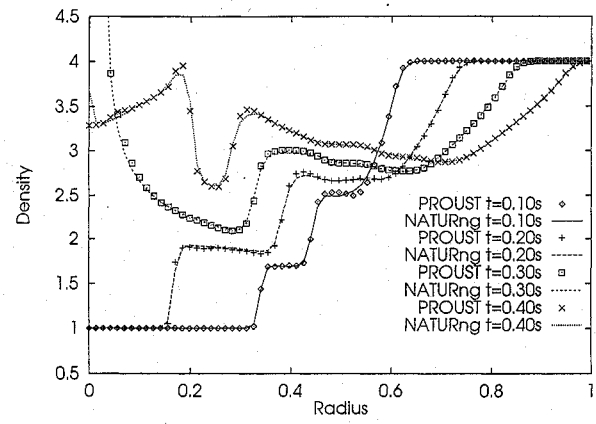

Fig. 11 Two-dimensional density profiles.

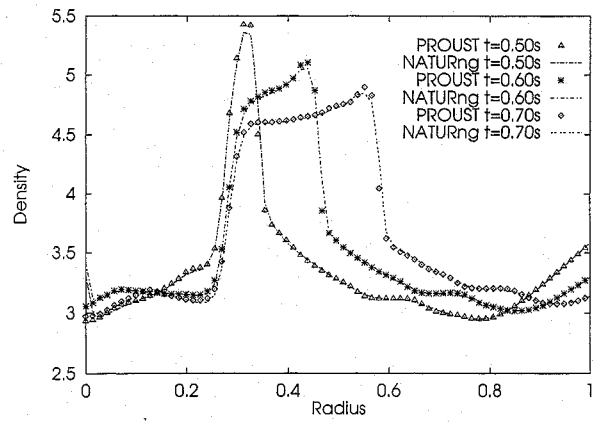

Fig. 12 Two-dimensional density profiles.

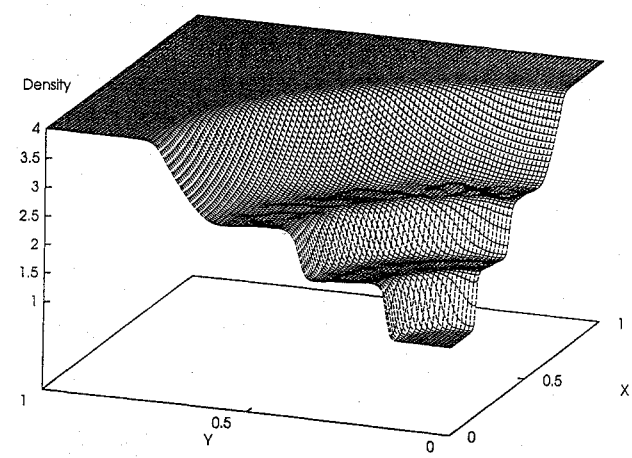

Fig. 13 Density contour at t = 0.20 s (NATURng).

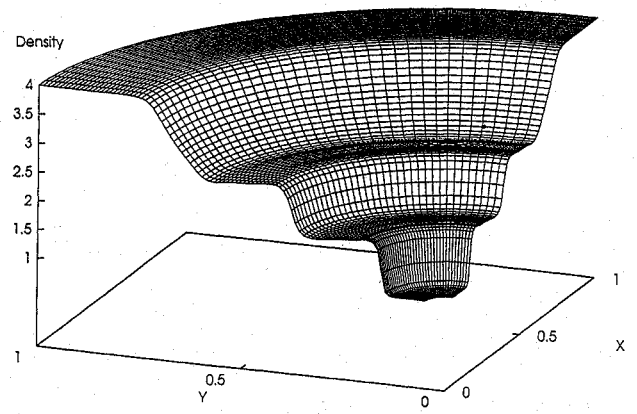

Fig. 14 Density contour at $t = 0.20$ s (radial mesh, PROUST).

decomposition of the convective flux applied entails that mesh position influences the speed of motion of strong waves. In the particular case of a circular wave discretized on an orthogonal grid, for angle variation from 0 to 90 deg, every possible orientation exists. Consequently, the predicted velocity of the wave front is not uniform, thus leading to the angular property variations. The nonuniformities increase with decreasing radius. The irregular integration cells used with NATURng, compared to the squares used with PROUST, lead to smoother, unstructured, ripples, but the computed amplitudes are alike. Likewise this drawback is related to a basic problem, and not to a specific hypothesis used in either method. It was verified that using a radial mesh eliminated the ripples (Fig. 14).

V. Conclusion

Two high-order upwind finite volume schemes for unsteady Euler solutions are described and compared. The first method, PROUST, implements the Van Leer flux vector splitting on structured grids and compatibility relations to treat boundary conditions. The second, NATURng, is based on the Roe's approximate Riemann solver on unstructured, finite element type meshes and uses standard explicit boundary treatment. Results for one-dimensional strong waves propagation and interaction show very good agreement between the two methods and the theoretical solution. In this configuration, the simulation of the reflection of a shock from a wall reveals the weakness of the second approach's slip wall treatment, which requires an estimate of the unsteady wall pressure. The more sophisticated technique used in PROUST solves this problem, plainly justifying extra development costs. On the other hand, a converging cylindrical shock test case was successfully calculated by the two schemes, with very similar results. Although different flux evaluations and integration cells are employed, the same sensitivity of wave propagation to mesh orientation resulted. This was related to the one-dimensional decomposition of the convective flux, a popular technique used by the two methods.

Acknowledgments

The authors acknowledge support from Centre National de la Recherche Scientifique, SNECMA, and METRAFLU. Thanks are due to the Centre de Compétence en Calcul Numérique Intensif team of Centre National Universitaire Sud de Calcul (Montpellier, France) where the structured computations were done. The numerical results presented are freely available from the authors who invite further comparisons (E-Mail: aubert@mecaflu.ec-lyon.fr).

References

[1]Yee, H. C., "A Class of High-Resolution Explicit and Implicit Shock-Capturing Methods," NASA TM-101088, Feb. 1989.

[2]Roe, P. L., "Characteristic-Based Schemes for the Euler Equations," *Annual Review of Fluid Mechanics*, Vol. 18, 1986, pp. 337–365.

[3]Van Leer, B., "Towards the Ultimate Conservative Difference Scheme V: a Second-Order Sequel to Gudonov's Method," *Journal of Computational Physics*, Vol. 32, No. 1, 1979, pp. 101–136.

[4]Parpia, I. H., "Van Leer Flux Vector Splitting in Moving Coordinates," *AIAA Journal*, Vol. 26, No. 1, 1988, pp. 113–115.

[5]Hirsch, C., *Numerical Computation of Internal and External Flows*, Vol. 2, Wiley, New York, 1988, pp. 362–364.

[6]Dervieuse, A., "Steady Compressible Euler Simulations using Unstructured Finite-Element Meshes," Lecture Series in Computational Fluid Dynamics, Von Karman Institute for Fluid Dynamics, 1985-04, March 1985.

[7]Roe, P. L., "Approximate Riemann Solvers, Parameters Vectors, and Difference Schemes," *Journal of Computational Physics*, Vol. 43, No. 2, 1981, pp. 357–371.

[8]Thompson, J. F., and Warzi, Z. U. A., *Numerical Grid Generation. Foundations and Applications*, North-Holland, Amsterdam, 1985, pp. 33–52.

[9]Mulder, W. A., and Van Leer, B., "Implicit Upwind Methods for the Euler Equations," AIAA Paper 83-1930, July 1983.

[10]Angrand, F., and Dervieux, A., "Some Explicit Triangular Finite Element Schemes for Euler Equations," *International Journal for Numerical Methods in Fluids*, Vol. 4, No. 8, 1984, pp. 749–764.

[11]Van Albada, G. D., Van Leer, B., and Roberts, W. W., "A Comparative Study of Computational Methods in Cosmic Gas Dynamics," *Astronomy and Astrophysics*, Vol. 108, No. 1, 1982, pp. 76–84.

[12]Bristeau, M. O., and Periaux, J., "Finite Element Methods for the Calculation of Compressible Viscous Flow Using Mesh Refinement," *Lecture Series in Computational Fluid Dynamics*, von Kármán Institute for Fluid Dynamics, March 1986.

[13]Pironneau, O., *Méthodes des éléments finis pour les fluides*, Masson, Paris, France, 1988.

[14]Stoufflet, B., "Résolution numérique des équations d'Euler des fluides parfaits compressibles par des schémas implicites en éléments finis," Ph.D. Thesis, Université Paris VI, Paris, Oct. 1984.

[15]Shapiro, A. H., *The Dynamics and Thermodynamics of Compressible Fluid Flow*, Vol. 2, Ronald, New York, 1954, pp. 1018–1028.

[16]Lapidus, A., "Computation of Radially Symmetric Shocked Flows," *Journal of Computational Physics*, Vol. 8, No. 1, 1971, pp. 106–118.

[17]Abarbanel, S., and Goldberg, M., "Numerical Solution of Quasi-conservative Hyperbolic Systems—The Cylindrical Shock Problem," *Journal of Computational Physics*, Vol. 10, No. 1, 1972, pp. 1–21.

[18]Sod, G. A., "A Numerical Study of a Converging Cylindrical Shock," *Journal of Fluid Mechanics*, Vol. 83, Pt. 4, 1977, pp. 785–794.

[19]Zhang, H. S., and So, R. M. C., "A Flux-Coordinate-Splitting Technique for Flows with Shocks and Contact Discontinuities," *Computers in Fluids*, Vol. 20, No. 4, 1991, pp. 421–442.

[20]Hirsch, C., *Numerical Computation of Internal and External Flows*, Vol. 2, Wiley, New York, 1988, pp. 475–483.